

## PAPER

Cite this: *Nanoscale*, 2020, **12**, 10842

# Multi-praseodymium-and-tungsten bridging octameric tellurotungstate and its 2D honeycomb composite film for detecting estrogen†

Yan Zhang, Jun Jiang, Yifan Liu, Pan Li, Yong Liu, Lijuan Chen\* and Junwei Zhao \*

Under coordination driving force of tungsten and rare-earth (RE) bridges, we synthesized a novel giant multi-tungsten-and-RE-bridging octameric tellurotungstate (TT)  $[H_2N(CH_3)_2]_{16}K_8Na_6H_{10}[Pr_8(H_2O)_{20}W_{16}O_{48}][B-\alpha-TeW_9O_{33}]_8 \cdot 70H_2O$  (**1**) in  $CH_3CN-H_2O$  mixed solvent. The cluster anion  $\{[Pr_8(H_2O)_{20}W_{16}O_{48}][B-\alpha-TeW_9O_{33}]_8\}^{40-}$  features sixteen  $W^{VI}$  bridges, eight  $Pr^{III}$  bridges and eight trivacant Keggin  $[B-\alpha-TeW_9O_{33}]^{8-}$  fragments, which the square  $\{W_4O_{12}\}$  cluster can be imagined as a seed to induce the aggregation of eight  $[B-\alpha-TeW_9O_{33}]^{8-}$  fragments by coordination driving force of additional twelve  $W^{VI}$  bridges and eight  $Pr^{III}$  ions. Furthermore, the 2D **1@DODA** (dimethyldioctadecyl ammonium bromide = DODA·Br) honeycomb composite material was prepared. The honeycomb morphology of the **1@DODA** composite material provides rich binding sites for electrodepositing Au nanoparticles to make Au/**1@DODA** electrodes. The aptamer of 17 $\beta$ -estradiol (E2) hormone can be grafted to the Au/**1@DODA** electrodes via Au–S bonding interaction to construct the Au/**1@DODA** aptamer biosensors. By virtue of the specific recognition interaction of aptamer and the electrochemical signal amplification function of methylene blue and cDNA, the Au/**1@DODA** aptamer biosensors can realize the electrochemical detection of E2. This finding not only offers an electrochemical biosensing platform for detecting E2, but also expands POM-based composite materials in the applications of clinical detection and biological analysis.

Received 6th March 2020,

Accepted 5th May 2020

DOI: 10.1039/d0nr01901a

rsc.li/nanoscale

## Introduction

2D nanomaterials have triggered extensive research enthusiasm because of their tuneable electronic structures, high specific surface areas with abundant exposed surface atoms and many potential applications in luminescence, catalysis, sensors and electronic devices.<sup>1–4</sup> Recently, a variety of materials such as graphene,  $WS_2$  and  $MoS_2$  have been considered as novel functional 2D nanomaterials.<sup>5–9</sup> Metal-oxide (MO) 2D porous nanomaterials, as a significant branch of 2D nanomaterials are still in their infancy.<sup>10</sup> Therefore, designing and preparing novel MO 2D porous nanomaterials remain a great challenge.

Polyoxometalates (POMs) are a group of nanosized MO clusters formed by condensation of  $\{MO_x\}$  polyhedral in the edge-, corner-, face-sharing fashions and have displayed a variety of applications in catalysis, medicine, magnetism, optics and

electrochemistry, *etc.*<sup>11–18</sup> Synthesizing gigantic poly(POM) aggregates containing different metal centers and further endowing them with unique 2D porous morphology by the functionalization method would offer great prospects. Among the treasury of POM architectures, some gigantic POM-based materials have been prepared through a one-step self-assembly strategy.<sup>19–26</sup> For example, in 2010, Cronin's group utilized  $SeO_3^{2-}$  as a template to construct a nanosized saddle-shaped  $[H_{34}W_{119}Se_8Fe_2O_{420}]^{54-}$  containing 119 W centers and 2  $Fe^{3+}$  ions.<sup>27</sup> In 2013, Su and co-workers isolated several giant rare-earth(RE)-containing poly(POM) aggregates containing eight vacant POM units in the help of  $SeO_3^{2-}$  and  $TeO_3^{2-}$  by a self-assembly strategy.<sup>19</sup> The bridging function of heteroatoms with unshared pair of electrons in polyoxotungstate system was also explored by our group and the  $Bi^{3+}$  ion was used for developing a giant cerium–bismuth tungstate nanocluster  $\{[W_{14}Ce^{IV}_6O_{61}][[W_3Bi_6Ce^{III}_3(H_2O)_3O_{14}][B-\alpha-BiW_9O_{33}]_3]_2\}^{34-}$  containing 104 metal centers.<sup>23</sup> However, up to now, only a few representative giant tungstotellurates (TTs) have been constructed by Cronin and Su's group *et al.*,<sup>19,20</sup> continuous exploration and preparation of giant poly(TT) clusters with manifold metal centers is still an important and challengeable research domain in POM field. To cope with this challenge, we decide to explore and synthesize novel giant multi-RE-and-

Henan Key Laboratory of Polyoxometalate Chemistry, College of Chemistry and Chemical Engineering, Henan University, Kaifeng, Henan 475004, China.

E-mail: ljchen@henu.edu.cn, zhaojunwei@henu.edu.cn

† Electronic supplementary information (ESI) available: The refinement details and additional figures. CCDC 1973217. For ESI and crystallographic data in CIF or other electronic format see DOI: 10.1039/d0nr01901a

tungsten bridging poly(TT) aggregates by the one-step self-assembly strategy of simple commercial materials of  $\text{K}_2\text{TeO}_3$ ,  $\text{Na}_2\text{WO}_4 \cdot 2\text{H}_2\text{O}$  and  $\text{RE}(\text{NO}_3)_3 \cdot 6\text{H}_2\text{O}$  in the presence of organic solubilizers based on the following considerations: (a) Multifunctional RE (herein is  $\text{Pr}^{3+}$ ) cations were employed in the reaction system because of their strong coordination ability and high coordination number, which are very helpful for linking *in situ* generated TT units into huge nanosized aggregates.<sup>28–31</sup> (b)  $\text{Na}_2\text{WO}_4 \cdot 2\text{H}_2\text{O}$  not only can participate in the construction of basic POM units in the self-assembly system, but also can serve as linking groups to integrate more POM units, which is helpful to stabilize the desired POM architectures.<sup>32–34</sup> Therefore, the excess dosage of  $\text{Na}_2\text{WO}_4 \cdot 2\text{H}_2\text{O}$  is essential in the process of constructing huge poly(POM) aggregates. (c) The lone pair of electrons on  $\text{TeO}_3^{2-}$  has the remarkable space stereochemistry effect, which makes the reaction of  $\text{TeO}_3^{2-}$  and  $\text{WO}_4^{2-}$  easily produce highly active lacunary TT fragments. The formation of these lacunary TT fragments provides good conditions for the incorporation of RE ions into the skeletons of lacunary TT fragments. (d) Dimethylamine hydrochloride was also used as an organic solubilizer since dimethylamine components not only can effectively reduce amorphous precipitates resulting from the rapid combination of RE cations and tungstates, but also are liable to be protonated in the acidic environment and form monoprotonated dimethylamine cations with larger volume than  $\text{K}^+$  and  $\text{Na}^+$  cations, which favour to stabilize the resulting larger RE-incorporated poly(POM) anions.<sup>35,36</sup> (e) The auxiliary mixed solution ( $\text{CH}_3\text{CN}:\text{H}_2\text{O} = 1:3$ ) was introduced into the one-step self-assembly system. On one hand, the organic-inorganic mixed solution is highly conducive to increase the solubility of organic solubilizer in aqueous solution, which is beneficial to stabilize complicated RE-containing TTs.<sup>37–39</sup> On the other hand, the fast volatility of  $\text{CH}_3\text{CN}$  can accelerate the agglomeration of basic POM units into unexpected architectures. Based on the above considerations, we obtained a novel sixteen-W-eight-Pr-incorporated octameric TT aggregate  $[\text{H}_2\text{N}(\text{CH}_3)_2]_{16}\text{K}_8\text{Na}_6\text{H}_{10}[\text{Pr}_8(\text{H}_2\text{O})_{20}\text{W}_{16}\text{O}_{48}][\text{B}-\alpha\text{-TeW}_9\text{O}_{33}]_8 \cdot 70\text{H}_2\text{O}$  (**1**) in mixed  $\text{CH}_3\text{CN}:\text{H}_2\text{O}$  solution and its cluster anion  $\{[\text{Pr}_8(\text{H}_2\text{O})_{20}\text{W}_{16}\text{O}_{48}][\text{B}-\alpha\text{-TeW}_9\text{O}_{33}]_8\}^{40-}$  features sixteen W<sup>VI</sup> and eight Pr<sup>III</sup> linkers as well as eight tri-vacant  $[\text{B}-\alpha\text{-TeW}_9\text{O}_{33}]_8^{8-}$  units.

Furthermore, although some gigantic molecular clusters have been fabricated, their application exploitations are relatively hysteretic due to their good water solubility and instability. Engineering gigantic molecular clusters into 2D functional nanomaterials could vastly enhance their stability and broaden their application fields. Recently, some methods have been proposed to prepare functional 2D porous MO-based nanomaterials, such as the layer-by-layer assembly strategy, the template-induced method and the Langmuir–Blodgett (LB) technology.<sup>40–43</sup> However, the pore sizes of 2D porous materials are difficult to control through the above synthetic strategies. Under these circumstances, the breath-figure (BF) method has been developed in recent years, which can be used to manufacture 2D honeycomb

morphology under a moist gas flow condition.<sup>44,45</sup> To date, there are some reports on POM-based honeycomb nanomaterials fabricated by the BF method, and the site-specifically electro-deposition of Au nanoparticles (NPs) in the pores of a 2D honeycomb was researched by Hao and his co-workers.<sup>46</sup> Recently, Au NPs modified aptamer biosensors have aroused immense interest owing to its prominent specificity and sensitivity.<sup>47</sup> Based on these ideas, we believe that POMs as giant MO nanoclusters can be also used to construct novel POM-based 2D honeycomb nanomaterial substrate, which can build up Au-modified aptamer biosensors toward detecting biomolecules. Nowadays, pharmaceutical contaminants have been a huge threat for organisms. The 17 $\beta$ -estradiol (E2) hormone exists widely in natural sources owing to its fattening, contraceptives and therapeutic effects for animals.<sup>48–51</sup> In this article, in the help of dimethyldioctadecyl ammonium bromide (DODA-Br), we employed the pre-synthesized sixteen-W-eight-Pr-incorporated octameric TT aggregate **1** to construct the 2D honeycomb porous materials by means of the BF method. Notably, the site-specifically electro-deposition of Au nanoparticles (NPs) in the pores of the 2D honeycomb **1@DODA** composite materials provides us a good chance to fabricate Au-modified **1@DODA** aptamer biosensors for detecting E2. The highly dispersed Au NPs on the pores of the POM-based honeycomb films are benefit for reducing the steric hindrance of large volume of aptamers of E2. In the assistance of methylene blue (MB) and cDNA as electrochemical signal amplifiers, we successfully realized the electrochemical detection of E2 and the detection limit (LOD) of the Au-modified **1@DODA** aptamer biosensor is  $3.58 \times 10^{-7} \mu\text{M}$ . To the best of our knowledge, this is the first POM-based Au-modified electrochemical aptamer biosensor. This work not only provides an electrochemical biosensing platform for detecting E2, but also opens a broad avenue for POM-based materials in clinical detection and biological analysis domain.

## Experimental

### Preparation of $[\text{H}_2\text{N}(\text{CH}_3)_2]_{16}\text{K}_8\text{Na}_6\text{H}_{10}[\text{Pr}_8(\text{H}_2\text{O})_{20}\text{W}_{16}\text{O}_{48}][\text{B}-\alpha\text{-TeW}_9\text{O}_{33}]_8 \cdot 70 \text{H}_2\text{O}$ (**1**)

$\text{K}_2\text{TeO}_3$  (0.602 g, 2.372 mmol) and  $\text{Na}_2\text{WO}_4 \cdot 2\text{H}_2\text{O}$  (4.684 g, 14.201 mmol) were dissolved in 20 mL mixed solvent ( $\text{CH}_3\text{CN}:\text{H}_2\text{O} = 1:3$ ). The pH was controlled at 3.0 by 6 mol  $\text{L}^{-1}$  HCl.  $\text{Pr}(\text{NO}_3)_3 \cdot 6\text{H}_2\text{O}$  (0.900 g, 2.069 mmol), dimethylamine hydrochloride (0.998 g, 12.239 mmol) were added to this solution with stirring. And then the pH was set back to 3.0 by using 4.0 mol  $\text{L}^{-1}$  NaOH. Heating the solution at 70 °C for 2 h and subsequently cooled and filtered. Green block crystals of **1** were isolated through slow evaporation for 3 days. Yield: 0.79 g (18.72% based on  $\text{Na}_2\text{WO}_4 \cdot 2\text{H}_2\text{O}$ ). Anal. calcd (%): H 1.23, C 1.47, N 0.85, Na 0.53, K 1.20, Te 3.91, Pr 4.31, W 61.90. Found: H 1.03, C 1.52, N 0.89, Na 0.36, K 1.09, Te 4.11, Pr 3.98, W 59.06. IR (KBr,  $\text{cm}^{-1}$ ): 3140 (s), 2785 (s), 1627 (s), 1466 (s), 965 (s), 870 (w), 785 (w), 702 (w).

### Preparation of the 1@DODA honeycomb film composite materials

According to previous literatures,<sup>44–46</sup> the general synthetic routes of the honeycomb film composite materials are divided in two steps. Initially, the non-water-soluble  $\text{CHCl}_3$  (20 mL) is opted to dissolve the cationic surfactant DODA·Br (41.190 mg, 0.065 mmol), and powdered **1** (50.0 mg) is dissolved in 10 mL deionized water. Both solutions are mixed together under tempestuously stirring overnight at room temperature. During this time, the positively-charged DODA<sup>+</sup> cations interact with the polyanions of **1** through electrostatic interaction and van der Waals interaction, leading to the **1**@DODA composite materials. On account of the solubility of aliphatic chains of DODA<sup>+</sup> cations in organic solvent, the **1**@DODA composite materials functionalized by aliphatic chains were successfully transferred to  $\text{CHCl}_3$  through fast phase transfer. After stopping stirring for a while, a clear phase interface emerged between  $\text{CHCl}_3$  and water. After the organic phase was separated, it was dried under 60 °C for about one day and cream-like **1**@DODA composite materials were obtained. Secondly, the **1**@DODA (1.0 mg) composite materials are re-dissolved in  $\text{CHCl}_3$  (1.0 mL) and the resulting solution (10  $\mu\text{L}$ ) is dropped onto a silicon slice in a humid environment. Because  $\text{CHCl}_3$  evaporates faster than water droplets, after water droplets evaporate for 20 min, numerous regular holes were formed on the surface of the **1**@DODA film composite materials, leading to its honeycomb-like micromorphology (Fig. 1a).

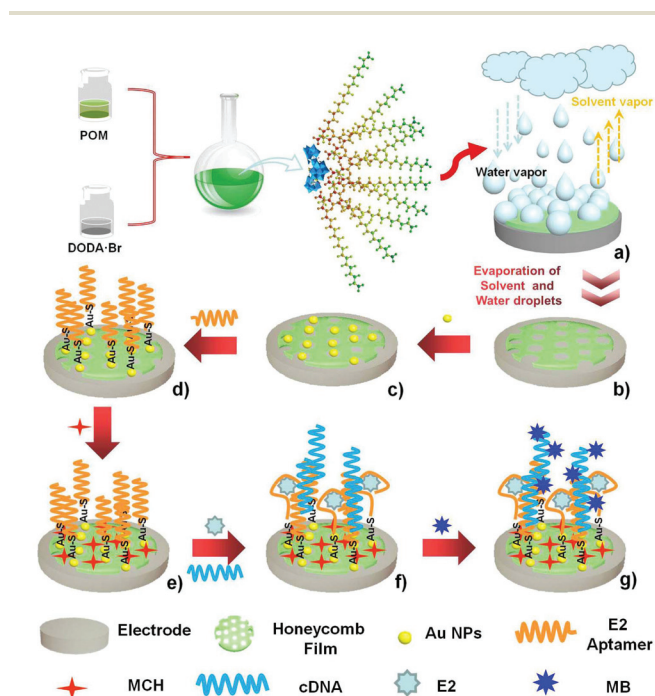


Fig. 1 (a) The formation scheme of the **1**@DODA honeycomb film composite material through the BF method. (b–g) Construction and detection mechanism of the **1**@DODA biosensor for detection of E2.

### Preparation of the Au-deposited **1**@DODA working electrodes

The glassy carbon electrodes were firstly polished using 0.05  $\mu\text{m}$  alumina powder, subsequently,  $\text{CHCl}_3$  solution (10.0  $\mu\text{L}$ ) containing 1  $\text{mg mL}^{-1}$  **1**@DODA was dropped onto the surface of the glassy carbon electrodes. The above glassy carbon electrodes were placed in a humid environment for 30 min, 2D honeycomb films were formed on the surface of the electrodes (named as the **1**@DODA electrodes) (Fig. 1b). The deposition of Au NPs on the **1**@DODA electrodes was performed by the amperometric  $i$ - $t$  measurement at a potential of  $-0.2$  V in the time range of 20–160 s in an aqueous solution containing 0.1 wt%  $\text{HAuCl}_4$  and 0.1 M  $\text{KNO}_3$  through the three-electrode system (the **1**@DODA working electrode, a Ag/AgCl reference electrode and a platinum counter electrode) (Fig. 1c). To find out the optimized time for site-specifically depositing Au NPs on the **1**@DODA electrodes (named as Au/**1**@DODA electrodes), pulse voltammetry (DPV), cyclic voltammetry (CV) and electrochemical impedance spectroscopy (EIS) measurements of the Au/**1**@DODA electrodes formed under different deposition times were performed in 10.0 mL aqueous solution containing 1.0 mM  $[\text{Fe}(\text{CN})_6]^{3/4-}$  and 0.1 M KCl solution.

### Preparation of the Au-modified **1**@DODA aptamer biosensors

The aptamer of E2 (8  $\mu\text{L}$ ) with different concentrations in the range of 0.05–0.15  $\mu\text{M}$  was respectively dropped onto the surface of Au/**1**@DODA electrodes (Fig. 1d). The functionalized Au/**1**@DODA electrodes by the aptamer of E2 (named as apt/Au/**1**@DODA electrodes) were kept for 12 h at room temperature so that the aptamer of E2 was anchored on each Au/**1**@DODA electrode through Au–S bond interaction. DPV measurements in 1.0 mM  $[\text{Fe}(\text{CN})_6]^{3/4-}$  and 0.1 M KCl solution manifest that the Au/**1**@DODA electrodes obtained in the presence of 0.11  $\mu\text{M}$  aptamer of E2 are the best. Subsequently, 6-mercapto-1-hexanol (MCH) (8  $\mu\text{L}$ , 1.0 mM) was dropped onto the surface of the best apt/Au/**1**@DODA electrodes (named as MCH/apt/Au/**1**@DODA electrodes) and then kept for 30 min to block the nonspecific binding sites of AuNPs (Fig. 1f). Next, different concentrations of E2 (8  $\mu\text{L}$ ) with 0.4  $\mu\text{M}$  cDNA are respectively dropped onto the MCH/apt/Au/**1**@DODA electrodes (named as E2(cDNA)/MCH/apt/Au/**1**@DODA electrodes). The E2(cDNA)/MCH/apt/Au/**1**@DODA electrodes were kept at 60 °C for 8 h to entail E2 or cDNA to be anchored to the electrodes by specific recognition interaction and base-complementary pairing interaction (Fig. 1g). Finally, the MB aqueous solution (8  $\mu\text{L}$ , 20  $\mu\text{M}$ ) was dropped onto the surface of each E2(cDNA)/MCH/apt/Au/**1**@DODA electrode and then kept for 10 min (Fig. 1h). The electrochemical signals were recorded in the 50.0 mM tris-HCl buffer solution (pH = 7.0) containing 20 mM KCl by the conventional three-electrode system.

## Results and discussion

### Structural description

X-ray diffraction structural analysis shows that **1** crystallizes in a tetragonal space group  $I4_1/a$  and its cluster anion

$\{\{\text{Pr}_8(\text{H}_2\text{O})_{20}\text{W}_{16}\text{O}_{48}\} [\text{B}-\alpha\text{-TeW}_9\text{O}_{33}]_8\}^{40-}$  (**1a**) is constructed from 8 trilacunary Keggin  $[\text{B}-\alpha\text{-TeW}_9\text{O}_{33}]^{8-}$  fragments, 16 additional bridging W centers and 8  $\text{Pr}^{3+}$  cations (Fig. 2a). Intriguingly, the octameric **1a** anion can be regarded as a three-shell structural assembly, which is similar to the reported three-shell  $\text{RE}_{14}$ -substituted structure of  $[(\text{RE}_{14}(\text{H}_2\text{O})\text{W}_4(\text{OH})\text{O}_{14})(\text{WO}_4)_4(\text{GeW}_{10}\text{O}_{38})_6]^{43-}$  (Fig. S1†).<sup>28</sup> In the center of the octameric **1a** anion, four  $\{\text{WO}_6\}$  groups are connected with each other in the vertex-sharing fashion to form a square  $\{\text{W}_4\text{O}_{12}\}$  cluster occupying the innermost shell of the octameric polyanion (Fig. 2b and c). All the W centers display the octahedral coordination geometry [W–O: 1.697(1)–2.477(8) Å and  $\angle\text{O–W–O}$ : 71.1(3)–172.8(5)°]. Whereas, in the  $[(\text{RE}_{14}(\text{H}_2\text{O})\text{W}_4(\text{OH})\text{O}_{14})(\text{WO}_4)_4(\text{GeW}_{10}\text{O}_{38})_6]^{43-}$  polyanion, four  $\{\text{WO}_6\}$  groups form a tetrahedral  $\{\text{W}_4\text{O}_{16}\}$  cluster in the vertex-sharing mode in the center of the polyanion (Fig. S1†).<sup>28</sup> These two  $\{\text{W}_4\text{O}_x\}$  clusters can be taken as a seed to grow a huge anionic cluster in the reaction system.

The second shell is a distorted cube established by eight  $\text{Pr}^{3+}$  cations, which are all located at the four vertices of the cube (Fig. 2b and d). In addition, each of them not only grafts to the innermost square shell, but also bridges the third shell that contains eight trivalent  $[\text{B}-\alpha\text{-TeW}_9\text{O}_{33}]^{8-}$  fragments to construct a huge octameric **1a** anion. It is worth noting that  $\text{Pr}^{3+}$  ions play an important bridging role in the construction of the whole structure and all the  $\text{Pr}^{3+}$  cations exhibit the

mono-capped square antiprism geometry with Pr–O distances of 2.388(8)–2.675(9) Å. A detailed description of the coordination configuration of each  $\text{Pr}^{3+}$  cation is provided in the ESI (Fig. S2†).

The third shell is made up of eight trilacunary Keggin  $[\text{B}-\alpha\text{-TeW}_9\text{O}_{33}]^{8-}$  fragments (Fig. 2b and e). Each of them links two bridging  $\{\text{WO}_6\}$  octahedra and one nine-coordinate  $\text{Pr}^{3+}$  ion through the oxygen atoms on the vacant position. The bridging function of the  $\{\text{WO}_6\}$  groups and  $\text{Pr}^{3+}$  ions enhances the stability of the whole **1a** anion. Furthermore, to reduce the steric hindrance, eight  $[\text{B}-\alpha\text{-TeW}_9\text{O}_{33}]^{8-}$  fragments are distributed in the staggered mode on both sides of the innermost shell of the  $\{\text{W}_4\text{O}_{12}\}$  cluster (Fig. 2a).

To further inspect the connection mode of **1a**, the skeleton of **1a** can be divided into two tetrameric  $\{\{\text{Pr}_4(\text{H}_2\text{O})_{10}\text{W}_6\text{O}_{18}\}[\text{B}-\alpha\text{-TeW}_9\text{O}_{33}]_4\}^{20-}$  (**1b**) subunits linked by one vertex-sharing  $\{\text{W}_4\text{O}_{12}\}$  cluster (Fig. 3a and b). **1b** can be considered as the fusion of two dimeric  $\{\text{Pr}_2(\text{H}_2\text{O})_5\text{W}_3\text{O}_9[\text{B}-\alpha\text{-TeW}_9\text{O}_{33}]_2\}^{10-}$  segments (Fig. 3c), in which it is apparent that the  $\text{Pr}^{3+}$  ions not only occupy the vacant positions of  $[\text{B}-\alpha\text{-TeW}_9\text{O}_{33}]^{8-}$  fragments, but also graft to the neighboring  $[\text{B}-\alpha\text{-TeW}_9\text{O}_{33}]^{8-}$  fragments through the terminal O atom from  $[\text{B}-\alpha\text{-TeW}_9\text{O}_{33}]^{8-}$  fragments (Fig. 3c). Of particular interest is that two dimeric  $\{\text{Pr}_2(\text{H}_2\text{O})_5\text{W}_3\text{O}_9[\text{B}-\alpha\text{-TeW}_9\text{O}_{33}]_2\}^{12-}$  subunits are aligned in a staggered pattern, which is conducive to reduce the steric hindrance as much as possible (Fig. 3d).

Furthermore, the dimeric  $\{\text{Pr}_2(\text{H}_2\text{O})_5\text{W}_3\text{O}_9[\text{B}-\alpha\text{-TeW}_9\text{O}_{33}]_2\}^{10-}$  subunit is composed of a “semilune”  $[\text{Te}_2\text{W}_{19}\text{O}_{68}]^{14-}$  moiety and a tetra-nuclear  $[\text{Pr}_2(\text{H}_2\text{O})_5\text{W}_2\text{O}_4]^{10+}$  cluster (Fig. 3e). The  $[\text{Te}_2\text{W}_{19}\text{O}_{68}]^{14-}$  moiety can be looked on

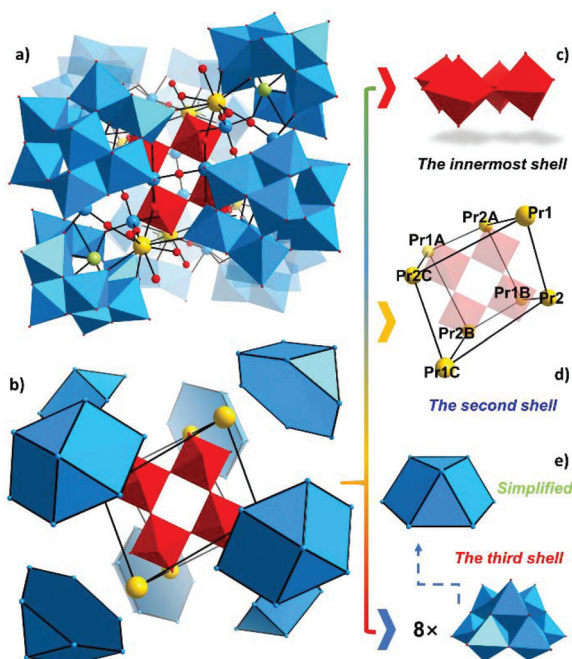


**Fig. 2** (a) Top view of the octameric **1a** anion. (b) The simplified three-shell configuration of **1a**. (c) The innermost  $\{\text{W}_4\text{O}_{12}\}$  shell of **1a**. (d) The simplified second shell of **1a**. (e) The third shell constructed from eight trilacunary Keggin  $[\text{B}-\alpha\text{-TeW}_9\text{O}_{33}]^{8-}$  fragments. The atoms with the suffixes A, B, and C are generated by symmetry operations where A denotes  $0.75 - y, 0.75 + x, -0.25 - z$ ; B denotes  $-0.75 + y, 0.75 - x, -0.25 - z$ ; C denotes  $-x, 1.5 - y, z$ .

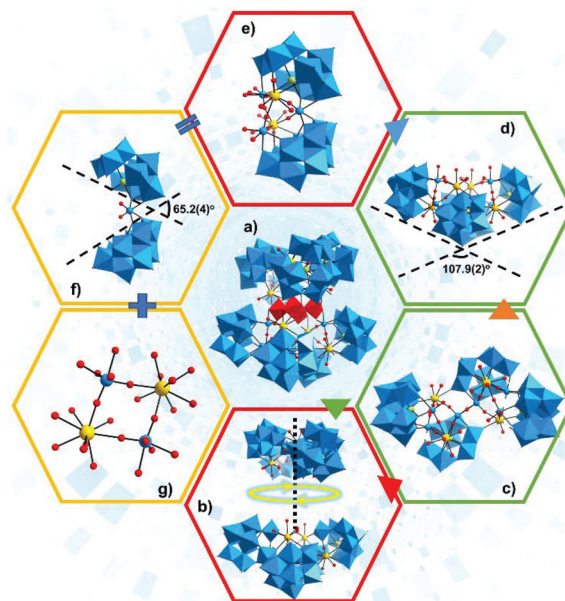


**Fig. 3** (a) Side view of the octameric **1a** anion. (b) Steric configuration of the two tetrameric **1b** subunits. (c) Top view of **1b**. (d) Side view of **1b**. (e) View of the dimeric  $\{\text{Pr}_2(\text{H}_2\text{O})_5\text{W}_3\text{O}_9[\text{B}-\alpha\text{-TeW}_9\text{O}_{33}]_2\}^{12-}$  segment. (f) View of the  $[\text{Te}_2\text{W}_{19}\text{O}_{68}]^{14-}$  moiety. (g) Linking mode between Pr and W centers in the tetra-nuclear  $[\text{Pr}_2(\text{H}_2\text{O})_5\text{W}_2\text{O}_4]^{10+}$  cluster.

as a derivative of two  $[\text{B-}\alpha\text{-TeW}_9\text{O}_{33}]^{8-}$  fragments bridged by one  $\{\text{WO}_6\}$  linker to give rise to a semilune configuration (Fig. 3f). The dihedral angle formed by two  $[\text{B-}\alpha\text{-TeW}_9\text{O}_{33}]^{8-}$  fragments is  $65.2(4)^\circ$ , which provides a wonderful chance to encapsulate the quadrangle tetra-nuclear  $[\text{Pr}_2(\text{H}_2\text{O})_5\text{W}_2\text{O}_4]^{10+}$  cluster (Fig. 3g) into the vacancy pocket.

Notably, the 3D stacking of **1** is orderly organized in all directions. Viewed along the *a* axis, the octameric **1a** anions present a –A–B–A–B– stacking pattern (Fig. S3a†). The arrangements in Layer A are two spatial orientations of **1a** anions and coincide with each other by a  $180^\circ$  rotation (Fig. S3b and c†). Layer B also displays a similar arrangement type. The staggered array of neighboring layers A and B in the crystal lattice greatly reduces the steric hindrance (Fig. S3d†).<sup>51</sup> Furthermore, the –A–B–A–B– stacking pattern can also be seen along the *b* axis, and the layer A almost overlaps with the layer B (Fig. S3e†). The steric hindrance is fully reduced by the staggered opposite spatial arrangements of layer A and layer B (Fig. S3f–h†). In addition, viewed along the *c* axis, **1a** anions are arranged by the –A–A–A– stacking pattern. In the *ab* plane, each polyanion **1a** coincides with the neighbouring polyanions by a  $180^\circ$  rotation (Fig. S3i and j†). Other else, crystal water molecules and  $[\text{H}_2\text{N}(\text{CH}_3)_2]^+$  counter cations fill in the gaps of **1a** anions through hydrogen-bonding interaction and electrostatic interaction with N–H...O distances of 2.68(4)–3.34(3) Å (Fig. S3k and l†).

Although the structure of the above-mentioned **1a** anion is very similar to that of  $[\{(\text{TeO}_3)\text{W}_{10}\text{O}_{34}\}_8\{\text{Ce}_8(\text{H}_2\text{O})_{20}\}(\text{WO}_2)_4(\text{W}_4\text{O}_{12})]^{48-}$  reported by Su's group,<sup>19</sup> the great disparity between them is that we introduced the  $[\text{H}_2\text{N}(\text{CH}_3)_2]^+$  organic species as counter cations into the structure of the huge nano-sized cluster by the one-pot assembly strategy, which is more conducive to the stability of the whole structure, and is helpful for cation exchange during the preparation process of the 2D honeycomb film. Moreover, it is the first time to apply the POM with complex and precise structure to construct the electrochemical aptamer biosensor. The polymetallic architecture may offer potential functions in detecting trace of E2 and

lay a foundation for broadening the application of POM frameworks.

### Characterization of the 2D **1@DODA** honeycomb composite material

Considering that 2D porous metal–oxide composite materials have sparked a great wave of enthusiasm because of the extraordinary physical and chemical properties in fundamental and technological applications, the 2D **1@DODA** honeycomb film composite material was prepared through the breath figure (BF) method and used as an aptamer carrier to construct electrochemical aptamer biosensors and detect traces of biomolecules in water source or human blood.

As for the BF method, the fast evaporation of organic solvent and the slow evaporation of water droplets facilitate the formation of the honeycomb morphology. In order to understand the micro-morphology of the material, SEM images of the 2D **1@DODA** honeycomb film composite material are illustrated in Fig. 4, it can be observed that the honeycomb film composite material with a uniform large-area porous structure was obtained (Fig. 4a). The enlarged SEM image exhibits that the honeycomb pores in the honeycomb film composite material are highly well-ordered (Fig. 4b and c). According to the statistical analysis, the distances between two neighbouring honeycomb pores are in the range of 2.0–3.5  $\mu\text{m}$  and the average diameter of the pores is *ca.* 4.8  $\mu\text{m}$  (Fig. 4d), which offers a good opportunity for evenly anchoring Au NPs to construct aptamer biosensor. Besides, the larger distances between two neighbouring honeycomb pores can effectively reduce steric hindrance of aptamers when the aptamers of E2 attach to the surface of Au NPs, so that more aptamers would graft to the working electrode for monitoring trace-concentration E2. Furthermore, EDS mapping images of Te, W, Pr, C, N and O elements of the honeycomb film composite material verify the successful combination of **1a** anions and  $\text{DODA}^+$  cations. As can be seen from Fig. 4e, the spatial distributions of Te, W, Pr, C, N and O elements in the honeycomb film composite material are uniform, further suggesting that

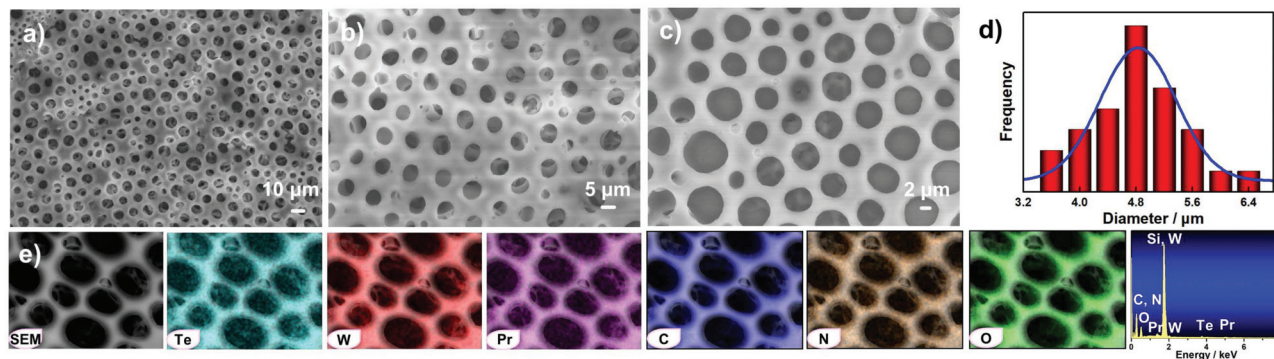
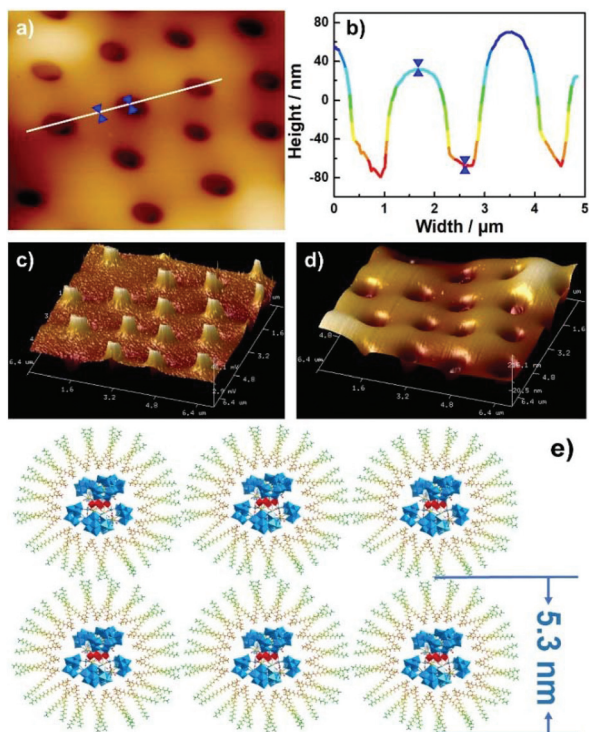


Fig. 4 (a) SEM image of the **1@DODA** honeycomb film composite material at a scale bar of 10  $\mu\text{m}$ . (b) SEM image of the **1@DODA** honeycomb film composite material at a scale bar of 5  $\mu\text{m}$ . (c) SEM image of the **1@DODA** honeycomb film composite material at a scale bar of 2  $\mu\text{m}$ . (d) The plot of pore size distribution of the **1@DODA** honeycomb film composite material. (e) EDS mapping and EDS images of the **1@DODA** honeycomb film composite material with Te, W, Pr, C, N and O elements.

DODA<sup>+</sup> cations and **1a** anions are successfully complexed by electrostatic interaction in the formation of honeycomb film composite material.<sup>46</sup> In addition, the TEM image of the honeycomb film composite material shows that the pores are bright, demonstrating the pores of the film are perforated (Fig. S4†). Unfortunately, there is no obvious observation of lattice fringe spacings by HRTEM because of the amorphous state of the composite material. Besides, the thickness of the film can be measured by means of atomic force microscope (AFM). The experimental results display that the thickness of the film is approximately 105 nm (Fig. 5a and b). What's more, the depths of holes in the honeycomb film composite material are uniform observed from the height plots (Fig. 5c and d). According to crystallographic data of **1**, the diameter of the **1a** anion is *ca.* 2.5 nm, while the length of the DODA<sup>+</sup> cation with planar zigzag conformation is estimated to be *ca.* 1.4 nm.<sup>52,53</sup> Considering the disordered conformation of the alkyl chains of DODA<sup>+</sup> cations and the distribution mode of DODA<sup>+</sup> cations around **1a** anions,<sup>54</sup> the **1@DODA** single-molecule layer should be less than 5.3 nm, thus it can be conjectured that the possible molecular layer number of the honeycomb film is less than 20 (Fig. 5e).

In order to explore the influence of organic solvents on the morphologies of the **1@DODA** composite materials, the non-



**Fig. 5** (a) 2D AFM image of the **1@DODA** honeycomb film composite material. (b) The thickness curve of the film composite material along with the line in Fig. 6a. (c) Height plot of the **1@DODA** honeycomb film composite material. (d) 3D AFM images of the **1@DODA** honeycomb film composite material with open pores. (e) Schematic illustration of the alkyl chains of DODA<sup>+</sup> cations with planar zigzag conformation surrounding **1a** anions.

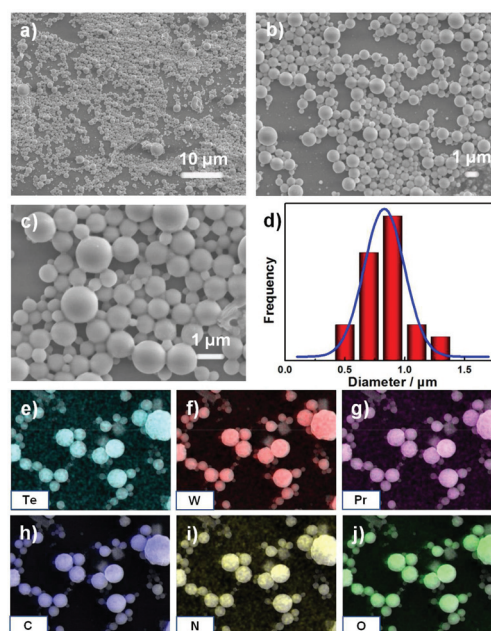


**Fig. 6** (a) SEM image of the **1@DODA** microspheres at a scale bar of 10  $\mu\text{m}$ . (b) SEM image of the **1@DODA** microspheres at a scale bar of 1  $\mu\text{m}$ . (c) SEM image of the **1@DODA** microspheres at a scale bar of 1  $\mu\text{m}$ . (d) The plot of pore size distribution of the **1@DODA** microspheres. (e–j) EDS mapping images of the **1@DODA** microspheres with Te, W, Pr, C, N and O elements.

water-soluble  $\text{CHCl}_3$  solvent was replaced by the water-soluble acetone solvent. The resulting products were characterized by SEM images. As can be seen from Fig. 6a, uniform **1@DODA** microspheres were obtained by using water-soluble organic solvent acetone (Fig. 6b and c). The diameters of the spheres are approximately 830 nm according to the statistical analysis (Fig. 6d). Moreover, EDS analyses exhibits that the Te, W, Pr, C, N and O elements are evenly distributed on the microspheres, which prove the successful combination of **1a** polyanions and DODA<sup>+</sup> cations (Fig. 6e–j). When  $\text{CHCl}_3$  was replaced by a water-soluble tetrahydrofuran, similar microspheres were obtained. However, when only water was used, large white amorphous deposits immediately form. These results indicate that insoluble organic solvents are important in the synthesis of 2D honeycomb film while water-soluble organic solvents tend to microscale spheres. Because of the site-specifically electro-deposition of Au NPs in the pores of the 2D honeycomb **1@DODA** composite, the 2D honeycomb **1@DODA** composite was further employed to construct biosensor towards E2.

In addition, the 2D **1@DODA** honeycomb layer in our work is somewhat different from the 2D layer assembling of Well-Dawson-POM structures featuring honeycomb porous framework on HOPG.<sup>55</sup> Several differences between them are found: (a) The organic media of constructing the 2D layers are different. In our work, we utilized non-water-soluble  $\text{CHCl}_3$  to prepare the 2D **1@DODA** composite material in a moist atmosphere. While the literature prepared a 2D layer by utilizing water-soluble acetonitrile. (b) The starting materials used for

preparing 2D layers are different. In our work, the 2D honeycomb layer is assembled from insoluble **1@DODA** composites formed by combing polyanion **1a** with DODA<sup>+</sup> cations through electrostatic interaction and van der Waals interaction. The amphipathic DODA<sup>+</sup> cations can be regarded as surfactants to encapsulate the surface of **1a** polyanions. In contrast, the literature utilized an amphipathic organically ligated V<sub>3</sub>-capped Wells–Dawson-type

{[HP<sub>2</sub>V<sup>V</sup><sub>3</sub>W<sup>VI</sup><sub>15</sub>O<sub>59</sub>((OCH<sub>2</sub>)<sub>3</sub>CCH<sub>2</sub>OCH<sub>2</sub>C<sub>6</sub>H<sub>4</sub>I)]} (WDI) to the 2D layer, which the triol organic ligand {(OCH<sub>2</sub>)<sub>3</sub>CCH<sub>2</sub>OCH<sub>2</sub>C<sub>6</sub>H<sub>4</sub>I}<sup>3-</sup> coordinates with the {V<sub>3</sub>} unit in the polar position of the tri-vacant Wells–Dawson-type {P<sub>2</sub>W<sub>15</sub>} subunit. The WDI in the literature is amphipathic whereas the **1@DODA** in our work is non-water-soluble. (c) The preparation methods of forming 2D layers are different. In our work, we utilized the BF method to synthesize 2D honeycomb film. The BF technique can be defined as a well-developed process of preparing an ordered porous film with condensed water droplets as the templates and employed by some reported literatures,<sup>45,46</sup> Because CHCl<sub>3</sub> evaporates faster than water droplets, after water droplets evaporating completely, numerous regular holes were formed on the surface of the **1@DODA** film, leading to its honeycomb-like micromorphology. While the literature used an acetonitrile solution to architecture a short-range-ordered porous molecular film. (d) The pore size and the height of the honeycomb layers are different. In our work, the average diameter of the pores is *ca.* 4.8 μm and the distances between two neighboring pores are in the range of 2.0–3.5 μm. Besides, the thickness of the film is approximately 105 nm. The **1@DODA** single-molecule layer is about 5.3 nm, thus it can be conjectured that the possible molecular layer number of the honeycomb film is less than 20. While in the literature, the porous molecular film is short-range-ordered and the height of the layer is around 800 pm, which is approximately to a WDI monolayer. The pore size of the porous layer is about 100 nm. The differences of their morphologies may be caused by the different preparation methods. (e) In the literature, the optimal construction experimental condition of the 2D layer is to utilize a waterless solvent with moderate polarity such as acetonitrile and small amounts of water in the main solvent will lead to the monomeric POM units to agglomerate to hierarchical micellar structures. These agglomerates seem to prevent the growth of expanded 2D layers on the surface. On the contrary, in our work, we use water droplets to form pores in the honeycomb film. The water droplets will not affect the morphology of **1@DODA** in CHCl<sub>3</sub> solution and interactions between **1@DODA** and the substrate. In addition, some inspiring knowledges can be learned. Different solvents especially for the mixed solvents can tailor different micelle structures. Therefore, we will further utilize the mixed solvents such as acetone-water, tetrahydrofuran-water and pure water solution to explore the **1/DODA** system and discover novel **1/DODA** composite materials with different morphologies and then investigate their electrochemical applications in clinical detection and biological analysis.

## Electrochemical performances of the Au-modified **1@DODA** aptamer biosensor

Recently, aptamer biosensors have attracted increasing attention due to the high selectivity and strong affinity to detecting targets.<sup>56,57</sup> However, few aptamer biosensors have been made by virtue of POM-based materials because most of them are soluble in aqueous solution, which greatly restricts them to be used as electrode materials and further hinders their applications in detecting trace substances.<sup>58,59</sup> Notably, the BF method can functionalize POMs to form a hydrophobic and porous 2D honeycomb film materials, moreover, Au NPs can be site-specifically electrodeposited into the pores of the 2D honeycomb film materials, which offer us an excellent opportunity to construct Au-modified POM-based aptamer biosensors to detect biological molecules.<sup>46</sup> Furthermore, some pharmaceutical contaminants such as E2 greatly threaten human health.<sup>60,61</sup> Herein, we have built a type of Au-modified **1@DODA** aptamer biosensors to monitor the E2 hormone in water source and human blood.

Initially, the **1@DODA** honeycomb film composite materials were modified on the polished glassy carbon working electrodes (the **1@DODA** electrodes). In order to evaluate whether the honeycomb film composite materials have been immobilized on the surface of the glassy carbon electrodes, DPV, CV and EIS measurements of the **1@DODA** electrodes were made in 1.0 mM [Fe(CN)<sub>6</sub>]<sup>3/4-</sup> and 0.1 M KCl solution (Fig. S5†). It can be clearly observed from Fig. S5a† that the DPV peak current of the **1@DODA** electrode is remarkably weaker than that of the bare glassy carbon electrode, the major reason of which is that the poor electrical conductivity of DODA<sup>+</sup> components in the **1@DODA** electrode leads to the decrease of the DPV peak current in comparison with the bare glassy carbon electrode. Similarly, the corresponding CV signal response of the **1@DODA** electrode is also dramatically weaker than that of the bare glassy carbon electrode (Fig. S5b†), and the EIS signal of the **1@DODA** electrode is larger than that of the bare glassy carbon electrode because of the poor electrical conductivity of DODA<sup>+</sup> components (Fig. S5c†). These observations demonstrate that the honeycomb film composite material has been successfully immobilized on the surface of the glassy carbon electrode.

Subsequently, Au NPs were site-specifically deposited into the honeycomb pores of the **1@DODA** electrodes to obtain the Au/**1@DODA** electrodes, which provide an indispensable condition for further combining the aptamer of E2 through Au–S bond interaction to manufacture Au-modified **1@DODA**-based aptamer-Au biosensors.<sup>62</sup> To find the optimal Au/**1@DODA** electrode, DPV, CV and EIS measurements of Au/**1@DODA** electrodes with different electrodeposition times of AuNPs in the range of 20–160 s have been performed in 1.0 mM [Fe(CN)<sub>6</sub>]<sup>3/4-</sup> and 0.1 M KCl solution, respectively (Fig. 7a and b). As illustrated in Fig. 7a and b, the DPV peak current of the Au/**1@DODA** electrodes gradually increases during increasing the electrodeposition time from 20 to 80 s, which may be that the gradual deposition of Au NPs into the honeycomb pores effec-

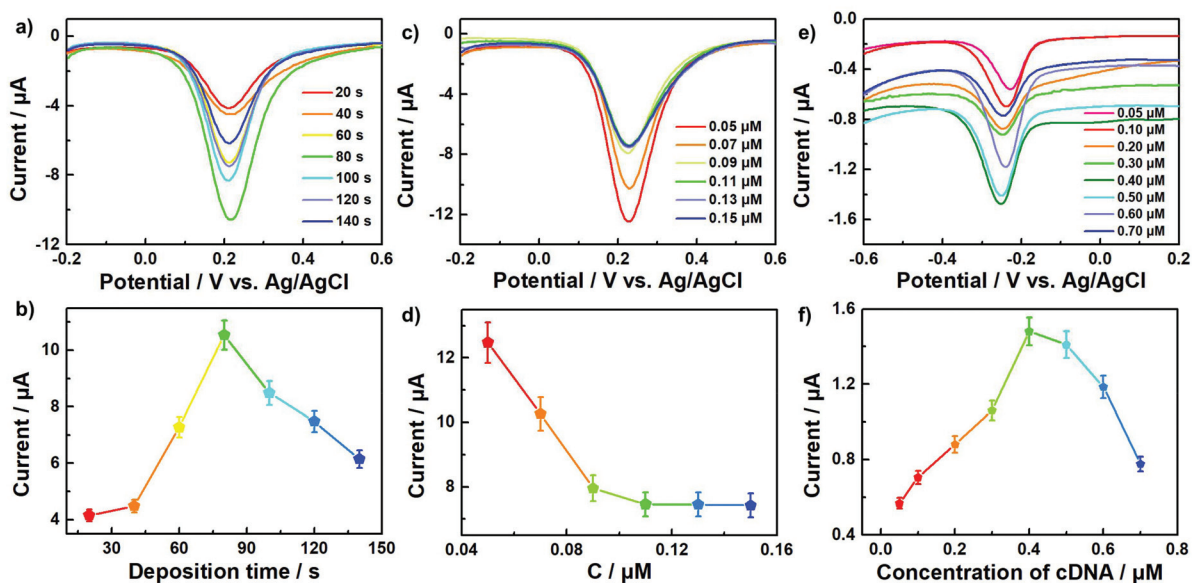


Fig. 7 (a) DPV curves of the Au/1@DODA electrodes prepared by controlling the electrodeposition time for 20, 40, 60, 80, 100, 120 and 140 s, respectively. (b) The DPV peak current intensity of the Au/1@DODA electrodes varying with the deposition time of Au NPs. (c) DPV curves of the Au/1@DODA-80 s electrodes obtained by incubating different concentration of aptamer of E2. (d) The DPV peak current intensity of the Au/1@DODA-80 s electrodes varying with the concentration of aptamer of E2. (e) DPV curves of the E2(cDNA)/MCH/Au/1@DODA electrodes with different concentrations of cDNA. (f) Comparison of the DPV peak current intensity of the E2(cDNA)/MCH/Au/1@DODA electrodes with different concentrations of cDNA.

tively enhances the electrical conductivity of the 1@DODA electrodes. However, further prolonging the electrodeposition time, the DPV peak current slowly decreases, the main reason of which is that the excessive deposition of Au NPs in the honeycomb pores of the 1@DODA electrodes results in the aggregation of Au NPs, which can impede the electron transfer between the surface of electrodes and the solution, thus leading to the decline of the DPV peak current.<sup>63</sup> Analogously, the evolution of CV curves of the Au/1@DODA electrodes also exhibits the same variation tendency (Fig. S6a†). With increasing the electrodeposition time of Au NPs, the CV peak current of Au/1@DODA electrodes gradually increases, whereas the current intensity descends when the electrodeposition time exceeds over 80 s. Correspondingly, the measured  $R_{ct}$  value of Au/1@DODA electrodes from the EIS measurements decreases when the electrodeposition time of Au NPs varies from 20 to 80 s whereas the  $R_{ct}$  value increases when the electrodeposition time increases from 80 to 160 s (Fig. S6b†). It can be concluded from the above analyses of DPV, CV and EIS measurements that the optimal electrodeposition time of Au NPs is 80 s for the preparation of the Au/1@DODA electrode (the Au/1@DODA electrode prepared under the optimal electrodeposition time condition is named as the Au/1@DODA-80 s electrode). Furthermore, the SEM image of the Au/1@DODA-80 s electrode is displayed in Fig. 8, as expected, from which it can be explicitly seen that Au NPs indeed have been deposited in the honeycomb pores of the 1@DODA-80 s electrode. These highly dispersed Au NPs in the pores of the 1@DODA-80 s electrode provide ample binding sites for attaching the aptamers of E2.

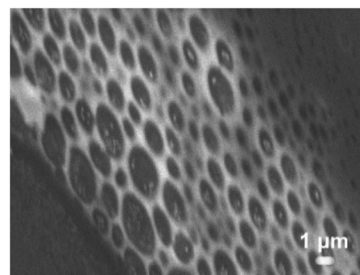


Fig. 8 The SEM image of the Au/1@DODA-80 s electrode.

After the aptamer of E2 was dropped onto the Au/1@DODA-80 s electrode and can covalently combine with the electrode by the Au-S bonding interaction. To find out an appropriate incubating concentration of the aptamer of E2 toward the Au/1@DODA-80 s electrode, the Au/1@DODA-80 s electrodes incubated by different concentrations of the aptamer of E2 were prepared and studied by making use of DPV, CV and EIS measurements in 1.0 mM  $[\text{Fe}(\text{CN})_6]^{3/4-}$  and 0.1 M KCl solution. It can be seen from Fig. 7c and d that the immobilization of the aptamer of E2 on the Au/1@DODA-80 s electrode leads to an apparent decrease of the DPV peak current because the electrostatic repulsion interaction between negatively charged phosphate backbone of the aptamer of E2 and  $[\text{Fe}(\text{CN})_6]^{3/4-}$  ions.<sup>64,65</sup> When the concentration of the aptamer of E2 exceeds 0.11  $\mu\text{M}$ , the DPV peak current drops down to a plateau, indicating that the aptamer of E2 has fully saturated the surface of the Au/1@DODA-80 s electrode by the Au-S

bonding interaction. Similarly, the CV curve evolution of the Au/1@DODA-80 s electrodes also reveals the same variation tendency (Fig. S6c†). In the meanwhile, the  $R_{ct}$  value of the Au/1@DODA-80 s electrodes increases when the concentration of the aptamer of E2 increases from 0.05  $\mu\text{M}$  to 0.11  $\mu\text{M}$  (Fig. S6d†) whereas the  $R_{ct}$  value remains almost unchanged upon further increasing the concentration of the aptamer of E2. Therefore, the optimum concentration of the aptamer of E2 incubating the Au/1@DODA-80 s electrodes is 0.11  $\mu\text{M}$  and this moment, the forming electrodes are named as the apt/Au/1@DODA-80 s electrodes. Moreover, in order to evidence the combination of Au NPs and the aptamer of E2 through Au-S bonds, the binding energy and the valence state of the sample were further analyzed by X-ray photoelectron spectroscopy (XPS). From the XPS spectra of apt/Au/1@DODA composite in Fig. S7,† the W, O, C, Au and S elements can be obviously observed due to the successful combination of 1@DODA, Au NPs and aptamer of E2. The Au 4f<sub>7/2</sub> and 4f<sub>5/2</sub> peaks appear at *ca.* 82.8 and 86.5 eV, respectively, being consistent with the Au<sub>0</sub> nucleus.<sup>66,67</sup> While the higher binding energies at about 83.8 eV and 87.7 eV are attributed to the formation of Au-S bonds on the surface of Au NPs.<sup>68,69</sup> The higher binding energies of Au in apt/Au/1@DODA compared with Au/1@DODA are caused by the lost electrons of Au NPs in apt/Au/1@DODA to bond with S atoms from the aptamer of E2. Meanwhile, the binding energy of S 2p is located at 162.9 eV, which corresponds to the Au-S bonds (Fig. S7e†).<sup>70,71</sup> The above phenomenon confirms the Au NPs are capped by the aptamer of E2 through Au-S bonds.

After the apt/Au/1@DODA-80 s electrodes were manufactured, MCH (8  $\mu\text{L}$ , 1.0 mM) solution was dropped onto the surface of each apt/Au/1@DODA-80 s electrode to block the nonspecific binding sites of AuNPs. However, E2 has no redox signals in the buffer, we should further utilize other materials with redox signals to assist the detection of E2. The sequence of cDNA not only can partially base-complementary with the aptamer of E2, but also has specific interaction with MB through the guanine groups on the cDNA. The organic dye MB belongs to the phenothiazine family and owns unique redox properties, which offers a good opportunity for us to detect E2. Thus, a mixed solution (8  $\mu\text{L}$ ) containing both cDNA and E2 was dropped onto each MCH/apt/Au/1@DODA-80 s electrode to offer the binding sites of MB for detecting E2. When the MCH/apt/Au/1@DODA-80 s electrodes were used to detect the testing solution containing both cDNA and E2, E2 can fully hybridize with the aptamer through stereospecific binding interaction and simultaneously reduces the binding opportunity of cDNA to the aptamer of E2, because cDNA is partially base-complementary pairing with the aptamer of E2 and the binding energy between cDNA and the aptamer of E2 is less than that between E2 and aptamer. When the concentration of E2 in the testing solution increases, the number of cDNA attached to the MCH/apt/Au/1@DODA-80 s electrode will decrease, thus resulting in a decrease of the number of MB grafted to the E2(cDNA)/MCH/apt/Au/1@DODA-80 s electrode, and the redox signals of MB will decline. On the contrary, when the concentration of cDNA in the testing solution

increases, the number of MB grafted on the E2(cDNA)/MCH/apt/Au/1@DODA-80 s electrode will increase and the redox signals of MB will be enhanced.<sup>62</sup> This is, the electrochemical signal response strength of the E2(cDNA)/MCH/apt/Au/1@DODA-80 s electrode is inversely proportional to the concentration of E2 in the testing solution.

To optimize the concentration of cDNA, different concentrations of cDNA ranging from 0.05 to 0.15  $\mu\text{M}$  in the presence of 0.01  $\mu\text{M}$  E2 were respectively dropped onto the surface of each MCH/apt/Au/1@DODA-80 s electrode and kept them at 60 °C for 8 h, giving rise to the E2(cDNA)/MCH/Au/1@DODA-80 s electrodes. Afterwards, MB (8  $\mu\text{L}$ , 20  $\mu\text{M}$ ) solution was dropped onto each E2(cDNA)/MCH/Au/1@DODA-80 s electrode and kept for 10 min. The electrochemical measurements of E2(cDNA)/MCH/Au/1@DODA-80 s electrodes were recorded in the 50.0 mM tris-HCl buffer solution (pH = 7.0) containing 20 mM KCl by the conventional three-electrode system. As can be seen from Fig. 7e-f, the redox signal of MB initially rises as increasing the concentration of cDNA, whereas the signal of MB decreases when the concentration of cDNA is higher than 0.4  $\mu\text{M}$ . Unfortunately, the charge transfer resistance of E2 and cDNA biomolecules was too large and no CV and EIS signals were detected after E2 or cDNA were anchored onto the MCH/Au/1@DODA-80 s electrodes. Thus, the solution containing 0.4  $\mu\text{M}$  cDNA and 0.01  $\mu\text{M}$  E2 was used to prepare the E2(cDNA)/MCH/Au/1@DODA-80 s electrodes (they can be named as 1@DODA biosensors). In the following experiments, only the DPV measurement was employed as a convenient tool for the detection of E2.

Under optimized conditions, a well-defined DPV peak current signal of MB in the sweeping range of -0.7 to 0.2 V was observed and utilized to detect the concentration of E2. As shown in Fig. 9a, the DPV peak current reveals a gradually weakening trend with increasing the concentration of E2 in the range of  $1.0 \times 10^{-4}$  to 1.0  $\mu\text{M}$ , which is because the increase of E2 suppresses the attachment of cDNA, further reduces the number of MB on the 1@DODA biosensors and leads to the decline of the DPV peak current. The fitting of the plot of the DPV peak current and the logarithm of the E2 concentration affords the regression equation:  $y = 0.1675x + 0.7168$  (Fig. 9b). Based on three times the standard deviation of the blank sample measurement (1).<sup>72,73</sup>

$$\text{LOD} = 3s/k \quad (1)$$

The standard deviation (*s*) can be calculated from three blank current intensity of the MB/cDNA/MCH/apt/Au/1@DODA-80 s electrode without any E2, the slope (*k*) is found to be 0.1675, and the corresponding regression coefficient  $R^2$  is 0.9629, the detection limit (LOD) was calculated as  $1.15 \times 10^{-7}$   $\mu\text{M}$ . The low LOD of detecting E2 may be attributed to the honeycomb porous structure of the 1@DODA composite material, which facilitates the dispersion of Au NPs and effectively reduces the crowding of biomolecules. In addition, although several findings on biomolecule detection based on the repulsion interaction between  $[\text{Fe}(\text{CN})_6]^{3/4-}$  ions and analytes have been reported, the weak detection current signals aren't conducive to data analysis.<sup>64,74,75</sup> In our work, using MB

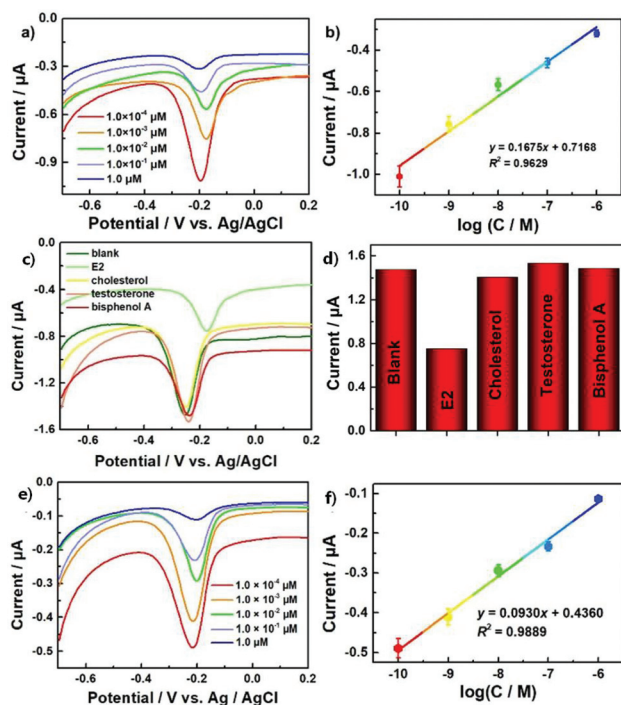


**Fig. 9** (a) DPV curves of the **1@DODA** biosensors prepared using different concentrations of E2. (b) The linear relationship of the DPV peak current intensity of the **1@DODA** biosensors with  $\log C_{E2}$ . (c) DPV curves of the **1@DODA** biosensors prepared using different concentrations of testosterone, 1-aminoanthraquinone, bisphenol A or cholesterol. (d) Comparison of the DPV peak current intensities of the **1@DODA** biosensors prepared using different concentrations of testosterone, 1-aminoanthraquinone, bisphenol A or cholesterol. (e) DPV curves of the **1@DODA** biosensors prepared using different concentration of E2 in 1000-fold diluted human serum solutions. (f) The linear relationship of the DPV current intensity of the **1@DODA** biosensors prepared in 1000-fold diluted human serum solutions with  $\log C_{E2}$ .

as a signal amplifier can effectively improve the detection current intensity and enhance the sensitivity of the **1@DODA** biosensor, which may be an effective method in the construction of biosensors.<sup>62</sup>

In addition, the selectivity is also an important indicator for evaluate the specific recognition of the **1@DODA** electrochemical biosensor. Therefore, several familiar biologics such as testosterone, 1-aminoanthraquinone, bisphenol A and cholesterol were used to examine the selectivity of the **1@DODA** biosensor. As can be seen from Fig. 9c, the DPV peak current signal of the **1@DODA** biosensor exhibits an obvious decrease tendency when detecting  $1.0 \times 10^{-4}$   $\mu\text{M}$  E2, while the peak currents only exhibit minor changes when detecting other biologics, because the aptamer of E2 owns the specific capture ability toward E2. Based on the above results, it is clearly seen that the highly selective detection ability of the **1@DODA** biosensor toward E2 and the proposed biosensor can be suitable for further detecting E2 in body fluids and water samples. To further apply the **1@DODA** biosensor to the actual sample detection, the **1@DODA** biosensors prepared using different concentration of E2 in 1000-fold diluted

**Table 1** Comparison of the sensitivity of different sensors for monitoring E2

Materials	LOD ( $\mu\text{M}$ )	Ref.
Au nanoparticles	$5.00 \times 10^{-2}$	48
Au nanoparticles	$2.00 \times 10^{-4}$	50
CoS/Au nanoparticles	$7.00 \times 10^{-7}$	63
Multiwalled carbon nanotubes (MWCNTs)/ $\beta$ -cyclodextrin ( $\beta\text{CD}$ )	$2.50 \times 10^{-3}$	76
<b>1@DODA</b> biosensors	$3.58 \times 10^{-7}$	Our work

human serum solutions were measured (Fig. 9e–f) and the function of the peak current *versus*  $\log C$  shows a linear relationship in the range of  $1.0 \times 10^{-4}$ – $1.0$   $\mu\text{M}$ , giving a LOD value of  $3.58 \times 10^{-7}$   $\mu\text{M}$  based on three times the standard deviation of the blank sample measurement. Compared with previous reports (Table 1), the novel **1@DODA** biosensors exhibits the good recognition performance toward E2, which indicates that POM-based biosensors may be practical for biomolecule detection application.

## Conclusions

In summary, we prepared a giant RE-containing TT **1** that incorporates sixteen  $\text{W}^{\text{VI}}$  bridges, eight  $\text{Pr}^{\text{III}}$  ions and eight trivalent Keggin fragments under coordination driving force of tungsten and praseodymium bridges in mixed solvent. Moreover, the reliable **1**-based aptamer biosensors for the detection of E2 were established. The good performances of the **1**-based aptamer biosensors were attributed to the following factors: (a) The unique 2D **1@DODA** composite material possesses a ordered honeycomb structure at the micrometer scale, which have plenty of well-ordered pores to site-specifically electro-deposition of Au NPs and provides a good opportunity for building up Au-decorated POM-based aptamer biosensors. (b) The larger distances between two neighboring honeycomb pores can effectively reduce steric hindrance of aptamers when the aptamers of E2 attach to the surface of Au NPs, so that more aptamers of E2 can graft to the biosensors for monitoring the trace-concentration E2. (c) Subsidiary MB and cDNA can amplify the detection signal of the **1@DODA** biosensor and enhance the sensitivity of the **1@DODA** sensor. This work not only present a multi-praseodymium-and-tungsten bridging octameric TT **1**, but also provides a useful platform for engineering POMs into nanosized materials to broad applicable potential of POM-based aptamer sensors in the fields of electrochemical detection and clinical testing and extends the application scopes of POM-based functional nanomaterials. We believe that this work might open a new avenue for using POM-based materials to detect biomolecules.

## Conflicts of interest

The authors declare that there are no conflicts to declare.

## Acknowledgements

This work was supported by the National Natural Science Foundation of China (21871077, 21671054, 21571048, 21771052), the Program for Innovation Teams in Science and Technology in Universities of Henan Province (20IRTSTHN004), the Program of First-Class Discipline Cultivation Project of Henan University (2019YLZDYJ02) and the Postgraduate Education Innovation and Quality Improvement Plan of Henan University (SYL18060130).

## References

- 1 F. Huang, Y. C. Deng, Y. L. Chen, X. B. Cai, M. Peng, Z. M. Jia, P. J. Ren, D. Q. Xiao, X. D. Wen, N. Wang, H. Y. Liu and D. Ma, *J. Am. Chem. Soc.*, 2018, **140**, 13142.
- 2 J. S. Hui, N. B. Schorr, S. Pakhira, Z. H. Qu, J. L. Mendoza-Cortes and J. Rodriguez-López, *J. Am. Chem. Soc.*, 2018, **140**, 13599.
- 3 T. Yu, Z. Y. Zhao, Y. H. Sun, A. Bergara, J. Y. Lin, S. T. Zhang, H. Y. Xu, L. J. Zhang, G. C. Yang and Y. C. Liu, *J. Am. Chem. Soc.*, 2019, **141**, 1599.
- 4 Y. Z. Li, X. M. Jiang, Z. H. Fu, Q. Q. Huang, G.-E. Wang, W.-H. Deng, C. Wang, Z. Z. Li, W. J. Yin, B. L. Chen and G. Xu, *Nat. Commun.*, 2020, **11**, 261.
- 5 L. T. Zhang, W. M. Kang, Q. Ma, Y. L. Jia, N. P. Deng, Y. Z. Zhang, J. Ju and B. Cheng, *J. Am. Chem. Soc.*, 2019, **141**, 13134.
- 6 K. S. Novoselov, A. K. Geim, S. V. Morozov, D. Jiang, Y. Zhang, S. V. Dubonos, I. V. Grigorieva and A. A. Firsov, *Science*, 2004, **306**, 666.
- 7 D. Chen, H. B. Feng and J. H. Li, *Chem. Rev.*, 2012, **112**, 6027.
- 8 M. Chhowalla, H. S. Shin, G. Eda, L.-J. Li, K. P. Loh and H. Zhang, *Nat. Chem.*, 2013, **5**, 263.
- 9 J. Pengm, Y. H. Liu, X. Luo, J. J. Wu, Y. Lin, Y. Q. Guo, J. Y. Zhao, X. J. Wu, C. Z. Wu and Y. Xie, *Adv. Mater.*, 2019, **31**, 1900568.
- 10 Y.-Y. Lyu, S. H. Yi, J. K. Shon, S. Chang, L. S. Pu, S.-Y. Lee, J. E. Yie, K. Char, G. D. Stucky and J. M. Kim, *J. Am. Chem. Soc.*, 2004, **126**, 2310.
- 11 S.-T. Zheng and G.-Y. Yang, *Chem. Soc. Rev.*, 2012, **41**, 7623.
- 12 L. Huang, S.-S. Wang, J.-W. Zhao, L. Cheng and G.-Y. Yang, *J. Am. Chem. Soc.*, 2014, **136**, 7637.
- 13 X.-B. Han, Z.-M. Zhang, T. Zhang, Y.-G. Li, W. Lin, W. You, Z.-M. Su and E.-B. Wang, *J. Am. Chem. Soc.*, 2014, **136**, 5359.
- 14 C. Boskovic, *Acc. Chem. Res.*, 2017, **50**, 2205.
- 15 S. Reinoso, M. Giménez-Marqués, J. R. Galán-Mascarós, P. Vitoria and J. M. Gutiérrez-Zorrilla, *Angew. Chem., Int. Ed.*, 2010, **49**, 8384.
- 16 B. S. Bassil, M. H. Dickman, I. Römer, B. von der Kammer and U. Kortz, *Angew. Chem., Int. Ed.*, 2007, **46**, 6192.
- 17 H. F. Shi, T. T. Zhao, Y. Zhang, H. Q. Tan, W. D. Wang, Y. G. Li and E. B. Wang, *Dalton Trans.*, 2019, **48**, 13353.
- 18 G. Yang, C. X. Wu, H. Q. Tan, X. J. Feng, L. K. Yan, H. Y. Zang and Y. G. Li, *J. Mater. Chem. A*, 2017, **5**, 765.
- 19 W.-C. Chen, H. L. Li, X.-L. Wang, K.-Z. Shao, Z.-M. Su and E.-B. Wang, *Chem. – Eur. J.*, 2013, **19**, 11007.
- 20 C. H. Zhan, J. M. Cameron, J. Gao, J. W. Purcell, D. L. Long and L. Cronin, *Angew. Chem., Int. Ed.*, 2014, **53**, 10362.
- 21 Q. Zheng, L. Vilà-Nadal, Z. L. Lang, J.-J. Chen, D.-L. Long, J. S. Mathieson, J. M. Poblet and L. Cronin, *J. Am. Chem. Soc.*, 2018, **140**, 2595.
- 22 J. Gao, J. Yan, S. Beeg, D.-L. Long and L. Cronin, *Angew. Chem., Int. Ed.*, 2012, **51**, 3373.
- 23 J.-C. Liu, Q. Han, L.-J. Chen, J.-W. Zhao, C. Streb and Y.-F. Song, *Angew. Chem., Int. Ed.*, 2018, **57**, 8416.
- 24 S. X. Shang, Z. G. Lin, A. X. Yin, S. Yang, Y. N. Chi, Y. Wang, J. Dong, B. Liu, N. Zhen, C. L. Hill and C. W. Hu, *Inorg. Chem.*, 2018, **57**, 8831.
- 25 N. Li, J. Liu, J.-J. Liu, L.-Z. Dong, S.-L. Li, B.-X. Dong, Y.-H. Kan and Y.-Q. Lan, *Angew. Chem., Int. Ed.*, 2019, **58**, 17260.
- 26 Y. Yang, T. Jia, Y.-Z. Han, Z.-A. Nan, S.-F. Yuan, F.-L. Yang and D. Sun, *Angew. Chem., Int. Ed.*, 2019, **58**, 12280.
- 27 J. Yan, J. Gao, D.-L. Long, H. N. Miras and L. Cronin, *J. Am. Chem. Soc.*, 2010, **132**, 11410.
- 28 Z. Li, X.-X. Li, T. Yang, Z.-W. Cai and S.-T. Zheng, *Angew. Chem., Int. Ed.*, 2017, **56**, 2664.
- 29 B. S. Bassil and U. Kortz, *Z. Anorg. Allg. Chem.*, 2010, **636**, 2222.
- 30 F. Hussain, R. W. Gable, M. Speldrich, P. Kögerler and C. Boskovic, *Chem. Commun.*, 2009, 328.
- 31 F. Hussain, F. Conrad and G. R. Patzke, *Angew. Chem., Int. Ed.*, 2009, **48**, 9088.
- 32 Y.-J. Wang, S.-Y. Wu, Y.-Q. Sun, X.-X. Li and S.-T. Zheng, *Chem. Commun.*, 2019, **55**, 2857.
- 33 J. Gao, J. Yan, S. Beeg, D.-L. Long and L. Cronin, *J. Am. Chem. Soc.*, 2013, **135**, 1796.
- 34 D. Wang, L. L. Liu, J. Jiang, L. J. Chen and J. W. Zhao, *Nanoscale*, 2020, **12**, 5705.
- 35 J. Yan, D.-L. Long and L. Cronin, *Angew. Chem., Int. Ed.*, 2010, **49**, 4117.
- 36 H. L. Li, Y. J. Liu, R. Zheng, L. J. Chen, J.-W. Zhao and G.-Y. Yang, *Inorg. Chem.*, 2016, **55**, 3881.
- 37 Z. J. Liang, D. D. Zhang, P. T. Ma, J. Y. Niu and J. P. Wang, *Chem. – Eur. J.*, 2015, **21**, 8380.
- 38 S.-T. Zheng, J. Zhang, X.-X. Li, W.-H. Fang and G.-Y. Yang, *J. Am. Chem. Soc.*, 2010, **132**, 15102.
- 39 D.-Y. Du, J.-S. Qin, S.-L. Li, Z.-M. Su and Y.-Q. Lan, *Chem. Soc. Rev.*, 2014, **43**, 4615.
- 40 E. Coronado and C. Mingotaud, *Adv. Mater.*, 1999, **11**, 869.
- 41 D. G. Kurth, P. Lehmann, D. Volkmer, A. Müller and D. Schwahn, *J. Chem. Soc., Dalton Trans.*, 2000, 3989.
- 42 M. Clemente-León, B. Agricole, C. Mingotaud, C. J. Gómez-García, E. Coronado and P. Delhaes, *Langmuir*, 1997, **13**, 2340.
- 43 S. Liu, Z. Tang, E. Wang and S. Dong, *Thin Solid Films*, 1999, **339**, 277.
- 44 D. W. Fan, X. F. Jia, P. Q. Tang, J. C. Hao and T. B. Liu, *Angew. Chem., Int. Ed.*, 2007, **46**, 9347.

- 45 W. F. Bu, H. L. Li, H. Sun, S. Y. Yin and L. X. Wu, *J. Am. Chem. Soc.*, 2005, **127**, 8016.
- 46 G. P. Zhang, H. X. Zhu, M. J. Chen, H. G. Li, Y. Yuan, T. T. Ma and J. C. Hao, *Chem. – Eur. J.*, 2017, **23**, 7278.
- 47 Y. Du and S. J. Dong, *Anal. Chem.*, 2017, **89**, 189.
- 48 O. A. Alsager, S. Kumar and J. M. Hodgkiss, *Anal. Chem.*, 2017, **89**, 7416.
- 49 S. U. Akki, C. J. Werth and S. K. Silverman, *Sci. Technol.*, 2015, **49**, 9905.
- 50 J. H. Soh, Y. Y. Lin, S. Rana, J. Y. Ying and M. M. Stevens, *Anal. Chem.*, 2015, **87**, 7644.
- 51 Y. J. Liu, H. L. Li, C. T. Lu, P. J. Gong, X. Y. Ma and L. J. Chen, *Cryst. Growth Des.*, 2017, **17**, 3917.
- 52 Y. Yan, B. Li, W. Li, H. L. Li and L. X. Wu, *Soft Matter*, 2009, **5**, 4047.
- 53 C. X. Tan, *J. Mol. Struct.*, 2017, **1148**, 34.
- 54 Y. Y. Li, X. F. Wu, Q. Y. Wu, H. Ding and W. F. Yan, *Dalton Trans.*, 2014, **43**, 13591.
- 55 M. Glöß, R. Pütt, M. Moors, E. Kentzinger, W. Pyckhout-Hintzen and K. Y. Monakhov, *Nanoscale*, 2019, **11**, 4267.
- 56 L. Shen, T. Bing, X. Liu, J. Wang, L. Wang, N. Zhang and D. Shangguan, *ACS Appl. Mater. Interfaces*, 2018, **10**, 2312.
- 57 P. P. Liu, X. Liu, X. H. Huo, T. Tang, J. Xu and H. Ju, *ACS Appl. Mater. Interfaces*, 2017, **9**, 27185.
- 58 P. Yin, D. Li and T. Liu, *Chem. Soc. Rev.*, 2012, **41**, 7368.
- 59 M. Sadakane and E. Steckhan, *Chem. Rev.*, 1998, **98**, 219.
- 60 L. Jiang, Y. Liu, S. Liu, X. Hu, G. Zeng, X. Hu, S. Liu, S. Liu, B. Huang and M. Li, *Chem. Eng. J.*, 2017, **308**, 597.
- 61 L.-H. Jiang, Y.-G. Liu, G.-M. Zeng, F.-Y. Xiao, X.-J. Hu, X. Hu, H. Wang, T.-T. Li, L. Zhou and X.-F. Tan, *Chem. Eng. J.*, 2016, **284**, 93.
- 62 K.-J. Huang, Y.-J. Liu, J.-Z. Zhang, J.-T. Cao and Y.-M. Liu, *Biosens. Bioelectron.*, 2015, **67**, 184.
- 63 X. Y. Lang, P. F. Guan, L. Zhang, T. Fujita and M. W. Chen, *Appl. Phys. Lett.*, 2010, **96**, 073701.
- 64 C.-S. Liu, Z.-H. Zhang, M. Chen, H. Zhao, F.-H. Duan, D.-M. Chen, M.-H. Wang, S. Zhang and M. Du, *Chem. Commun.*, 2017, **53**, 3941.
- 65 R. Hu, W. Wen, Q. L. Wang, H. Y. Xiong, X. H. Zhang, H. S. Gu and S. F. Wang, *Biosens. Bioelectron.*, 2014, **53**, 384.
- 66 W. Zhang, F. H. Li, Y. W. Hu, S. Y. Gan, D. X. Han, Q. X. Zhang and L. Niu, *J. Mater. Chem. B*, 2014, **2**, 3142.
- 67 Z. Wang, Q. Zhang, D. Kuehner, X. Xu, A. Ivaska and L. Niu, *Carbon*, 2008, **46**, 1687.
- 68 Y.-H. Wang, K.-J. Huang, X. Wu, Y.-Y. Ma, D.-L. Song, C.-Y. Du and S.-H. Chang, *J. Mater. Chem. B*, 2018, **6**, 2134.
- 69 H.-H. Deng, L.-N. Zhang, S.-B. He, A.-L. Liu, G.-W. Li, X.-H. Lin, X.-H. Xia and W. Chen, *Biosens. Bioelectron.*, 2015, **65**, 397.
- 70 F. Nakamura, E. Ito, T. Hayashi and M. Hara, *Colloids Surf., A*, 2006, **284**, 495.
- 71 A.-L. Morel, R.-M. Volmant, C. Méthivier, J.-M. Krafft, S. Boujday and C.-M. Pradier, *Colloids Surf., B*, 2010, **81**, 304.
- 72 P. Samanta, A. V. Desai, S. Sharma, P. Chandra and S. K. Ghosh, *Inorg. Chem.*, 2018, **57**, 2360.
- 73 P. Zhang, J. Jiang, R. Yuan, Y. Zhuo and Y. Q. Chai, *J. Am. Chem. Soc.*, 2018, **140**, 9361.
- 74 A. B. Iliuk, L. H. Hu and W. A. Tao, *Anal. Chem.*, 2011, **83**, 4440.
- 75 K. Saha, S. S. Agasti, C. Kim, X. N. Li and V. M. Rotello, *Chem. Rev.*, 2012, **112**, 2739.
- 76 A. U. Alam, Y. H. Qin, M. Catalano, L. H. Wang, M. J. Kim, M. M. R. Howlader, N.-X. Hu and M. J. Deen, *ACS Appl. Mater. Interfaces*, 2018, **10**, 21411.